Atmos. Meas. Tech. Discuss., 8, 2409–2436, 2015
www.atmos-meas-tech-discuss.net/8/2409/2015/
doi:10.5194/amtd-8-2409-2015
© Author(s) 2015. CC Attribution 3.0 License.

Atmospheric Measurement Techniques Discussions
Open Access

This discussion paper is/has been under review for the journal Atmospheric Measurement Techniques (AMT). Please refer to the corresponding final paper in AMT if available.

A cautionary use of DCC as a solar calibration target: explaining the regional difference in DCC reflectivity

M.-J. Choi and B. J. Sohn

School of Earth and Environmental Sciences, Seoul National University, Seoul, 151-747, Korea

Received: 14 November 2014 – Accepted: 16 February 2015 – Published: 4 March 2015

Correspondence to: B. J. Sohn (sohn@snu.ac.kr)

Published by Copernicus Publications on behalf of the European Geosciences Union.

Abstract

This study attempted to explain why deep convective clouds (DCCs) over the western Pacific are generally darker than those found over tropical African and South American land regions. For defining 1 km pixel DCCs in this study, 205 K of Aqua-MODIS brightness temperature at 11 µm (TB_{11}) was used as a criterion. Corresponding MODIS-measured reflectivities at 0.645 µm were examined, and an analysis of collocated Cloud Profile Radar (CPR) onboard CloudSat and Cloud Aerosol Lidar Infrared Pathfinder Satellite Observation (CALIPSO) measurements and derived cloud products was conducted.

From an analysis of the four January months of 2007–2010, a distinct difference in ice water path (IWP) between the western Pacific and the two tropical land regions was demonstrated. Small but meaningful differences in the effective radius were also found. The results led to a conjecture that smaller IWP over the western Pacific than over the tropical land regions is the main cause of smaller reflectivity there. This finding suggests that regionally different reflectivity of DCCs over the tropics up to 5 % on average are to be counted when those DCCs are used for the solar channel calibration.

1 Introduction

Vicarious calibrations for solar channels are particularly important for geostationary weather satellites that are not usually equipped with an onboard calibration system for the visible sensor, in order to assure the radiometric quality of satellite measurements. There are a variety of vicarious calibration methods in this end using different targets such as bright desert targets (Govaerts and Clerici, 2004; Miesch et al., 2003; Chun et al., 2012; Chun and Sohn, 2014), cloud targets (Kim et al., 2013; Ham and Sohn, 2010; Doelling et al., 2010; Sohn et al., 2009), and moon targets (Cao et al., 2009; Barnes et al., 2004). Amongst different approaches the use of deep convective cloud (DCC) targets is interesting because DCCs are highly reflective and thus can serve as

AMTD
8, 2409–2436, 2015

a natural diffuser (Sohn et al., 2009; Doelling et al., 2013a, b; Stercks et al., 2013). Since DCCs are abundant throughout the tropical belt and seasons alike there should be excellent advantage that all different sensors onboard geostationary satellites may be calibrated using DCC targets. For this, however, underlying assumption is that DCCs have radiatively similar behaviors.

However, a recent study by Doelling et al. (2013a), based on an analysis of Moderate Resolution Imaging Spectroradiometer (MODIS) solar channel measurements, reported that DCCs over the tropical western Pacific have lower reflectivity (or are darker) than DCCs over continental tropical regions such as Africa and South America. This suggests that simple adoption of DCC approach may result in erroneous calibration result.

In this study, with the goal of understanding why DCCs over the western Pacific show generally lower reflectivity in comparison with those over tropical African and South American regions, regional differences in optical properties of DCCs are examined using CloudSat Cloud Profile Radar (CPR) and Cloud Aerosol Lidar Infrared Pathfinder Satellite Observation (CALIPSO) measurements. From an intercomparison of the vertical structures of DCC optical properties, important elements causing regional differences in DCC reflectivity are identified. The obtained results may lead to a better understanding of the role of tropical DCCs in the use of DCC targets for the solar channel calibration.

2 Data and methodology

2.1 MODIS, CloudSat, and CALIPSO measurements

MODIS is a passive imager having 36 spectral bands that cover the visible and infrared spectrum. In this study, brightness temperature at 11 μm (TB_{11}) and reflectivity at 0.645 μm ($Ref_{0.6}$) converted from MODIS-measured radiances (MYD021 products; Collection-5 version) are used to define DCC and to examine characteristic reflec-

AMTD
8, 2409–2436, 2015

tivity features, respectively. MODIS-derived cloud parameters such as cloud optical thickness (COT) and column-integrated effective radius (R_e) are obtained from MYD06 products in order to analyze differences in cloud parameters between land and ocean regions in interest. All data are from MODIS Aqua products (http://ladsweb.nascom.nasa.gov/data/search.html).

CloudSat carries an active sensor called CPR that measures vertical profiles of reflectivity due to atmospheric hydrometeors at 94 GHz. The CloudSat 2B-GEOPROF product provides radar reflectivity and cloud mask information for 125 height bins. Because a cloud mask value of 30 is considered to be a threshold ensuring cloud presence in a given layer (Mace et al., 2007), CloudSat profiles are selected for analysis if the cloud mask value is greater than 30. Beside the use of reflectivity profiles, CloudSat-retrieved cloud parameters are used. These include cloud water content and effective radius profiles obtained from CloudSat 2B-CWC-RVOD products whose pixel resolution is about 1.4 km (Wood, 2008). However, because CloudSat-derived liquid water content and liquid effective radius are erroneous as the result of miscalculation of the attenuation by liquid cloud droplets (as of 21 Sept 2011, the CloudSat Data Processing Center listed on its website the "2B-CWC-RVOD 008 issue: radar forward model attenuation in liquid cloud," which is available online at http://www.cloudsat.cira.colostate.edu/dataIssue.php?prodid=6&pvid=227&anomalyid=325230) and those problems were not yet corrected by the time to write this paper, only ice water content (IWC) and ice effective radius (R_e) profile data were used in this study to examine the reflectivity difference. Because the visible extinction coefficient (k_{ext}) is closely linked to the optical thickness and visible reflectivity observable at top of atmosphere (TOA), the k_{ext} profile is estimated as follows (e.g., Lin and Rossow 1994; Ham and Sohn 2012):

$$k_{ext} = \frac{3}{4}\frac{Q_e}{\rho_i}\frac{IWC(z)}{R_e(z)} \quad (1)$$

AMTD
8, 2409–2436, 2015

In Eq. (1), extinction efficiency (Q_e) is considered to be nearly equal to 2 in the visible range, and density of ice crystals (ρ_i) is fixed as a constant (i.e., 0.917 g m^{-3}), as used in CloudSat retrieval.

CALIPSO also carries an active sensor, Cloud–Aerosol Lidar with Orthogonal Polarization (CALIOP), beaming at 532 and 1064 nm wavelengths and sensitive to particles much smaller than those detectable by CloudSat. Because CloudSat misses the top portion of DCC composed of small ice crystals (Kahn et al., 2008), CALIPSO data are used for information on cloud properties above the CloudSat-detected upper boundary of the reflectivity profile. In this study, CALIPSO-derived cloud parameters such as extinction coefficient at 0.532 µm (Young and Vaughan 2009) and ice water content (Heymsfield et al., 2005) profiles (CALIPSO L2-05kmCPro, Edition 3.01) are analyzed. It is a 5 km average based on the average of 15 CALIOP FOV of 100 m laser shots.

2.2 Construction of collocation data

Collocated data from Aqua MODIS, CloudSat, and CALIPSO, which compose the A-train mission (Stephens et al., 2002; Parkinson 2003; Winker et al., 2003), are constructed. However, because of the different MODIS scan geometry, measuring a much wider region, nadir-viewing scenes of MODIS measurements are collocated with CloudSat and CALIPSO measurements in about a 1 km field of view. Collocation is carried out over the along-track of CloudSat by selecting the closest MODIS and CALIPSO pixels from a given CloudSat pixel. The combination of collocated CloudSat, CALIPSO, and MODIS data will provide us overall features of the physical/optical properties of DCCs, from which key factors contributing to the regional difference in DCC reflectivity can be examined.

2.3 Analysis domain and period

In order to examine the regionally different optical properties of DCCs, three analysis areas are selected (Fig. 1), i.e., continental Central Africa (20° N–20° S, 0–40° E), South

AMTD
8, 2409–2436, 2015

America (10° N–30° S, 40–70° W), and the oceanic western Pacific (20° N–20° S, 100–180° E). Collocation data of Aqua MODIS, CloudSat, and CALIPSO measurements are constructed for the four January months in the 2007–2010 period. January is chosen because it is the time of year when DCCs are frequently observed over all three analysis regions.

2.4 DCC data

The DCCs of interest in this study are defined as optically thick clouds with top heights reaching higher than 14 km associated with strong convection resulting in cold cloud-top temperatures. Because of such high-altitude cloud tops, TB_{11} has often been used as a criterion determining the presence of DCCs. TB_{11} thresholds ranging from 190–210 K have been used for different DCC-related study objectives (e.g., Aumann et al., 2007; Liu et al., 2007; Sohn et al., 2009). The sensitivity of the TB_{11} threshold to measured visible radiance was tested by Doelling et al. (2013a), and the lowest radiances of DCCs, among the three selected regions of Fig. 1, were found over the western Pacific, especially when MODIS pixels of $TB_{11} < 205$ K were chosen as DCCs. In this study, the same TB_{11} of 205 K is used as the threshold to determine DCCs.

To avoid DCC targets located near the cloud edge or DCCs related to small-scale cloud plumes, spatial homogeneity is applied to the distribution of TB_{11} and $Ref_{0.6}$. A selected pixel is identified as a DCC target if the 9 × 9 MODIS pixels (corresponding to about 10 km × 10 km) surrounding the CloudSat pixel show a SD of TB_{11} of less than 1 K. The spatial homogeneity criterion is also applied for visible reflectivity. The pixel is selected if the SD of the $Ref_{0.6}$ from the surrounding 9 × 9 pixels normalized by the mean value is less than 0.03. Collocation targets are selected only if both criteria are satisfied. The confidence level of the collocation is enhanced by restricting the solar zenith angle (SZA) and satellite viewing zenith angle (VZA) to less than 40°. Furthermore, only single-layered cloud, which can be determined from the vertical structure of CloudSat radar reflectivity, is retained in this DCC analysis.

AMTD
8, 2409–2436, 2015

The total numbers of pixels passing the aforementioned criteria are 285, 687, and 2377 for Africa, South America, and the western Pacific region, respectively. The number of DCC pixels collected for each month is given in Table 1. Considering that the western Pacific domain size is about twice the size of the two land regions, DCCs are found to be more abundant over the western Pacific region compared to the two land regions. It is also interesting to note that the African domain seems to show a more fluctuating interannual pattern over the four-year period.

3 Optical properties of DCCs

3.1 MODIS measurements

First, statistical distributions of selected DCC pixels are compared with one another for the three regions. In doing so, probability density functions (PDFs) of MODIS-measured TB_{11}, $Ref_{0.6}$, MODIS-derived COT, and R_e are obtained and are presented in Fig. 2. PDFs for TB_{11} (Fig. 2a) show generally decreasing frequency with decreasing temperature. The more fluctuating patterns found in the two land regions may be, in part, due to the relatively smaller sample size (shown in Table 1). Interestingly, extremely cold TB_{11} (lower than 190 K) is found more frequently over the western Pacific (black solid line), although the total frequencies are very small (less than 3 % of the sample size). Consequently, warmer TB_{11} appears to be more frequent (in percentage) over the land regions of Africa and South America.

Corresponding reflectivity distributions are shown in Fig. 2b. The western Pacific region shows a more widely distributed pattern, with a reflectivity peak around 0.98, compared to the two land regions. On the contrary, the two land regions exhibit patterns shifted to higher reflectivity, with a more dominant probability at a peak reflectivity of about 1. It is clear that DCCs found over the western Pacific are generally darker than those found over tropical Africa and South America; their mean values are 0.93, 0.98, and 0.98, respectively (Table 2). By combining these with the patterns noted

AMTD
8, 2409–2436, 2015

in TB_{11} distributions, the DCCs over the two tropical land regions can be characterized as clouds that show warmer cloud tops along with higher reflectivity compared to those in the western Pacific: 199.6 K (Africa) and 200.2 K (South America) vs. 198.8 K (western Pacific) (Table 2). These results are consistent with the findings of Doelling et al. (2013a).

PDFs of MODIS-derived COT and R_e are given in Fig. 2c and d, respectively. Because the MODIS cloud algorithm only provides COT up to 100 even if clouds are thought to be optically thicker than 100 and because DCCs having COT = 100 occupy 69.5, 71.5 %, and 49.0 % of the DCCs for Africa, South America, and the western Pacific domains, respectively, the dominant portion of PDFs should be located near COT = 100. Thus, separate plots are made for COT < 100 and for COT > 90. As shown in Fig. 2b, the majority of DCCs over the two land regions show DCCs with reflectivity (i.e. bidirectional reflectance based on the Lambertian assumption) higher than or equal to 1. In contrast, about half of the DCC samples over the western Pacific show COT > 100, indicating that the DCCs found over the western Pacific are optically thinner than those of the two land counterparts. Furthermore, considering that remaining 50 % of DCC pixels are more evenly distributed throughout the covered COT range, the DCCs determined by applying only the criteria of TB_{11} = 205 K may have contained more optically thinner convective/anvil-type clouds. DCC samples that are possibly contaminated by optically thinner clouds over the western Pacific may have caused the lower reflectivity there. However, even when we remove possible contaminated scenes (e.g., reflectivity lower than 0.95), the average of highly reflective clouds (i.e., $Ref_{0.6} > 0.95$) is higher in the land regions: 0.99, 1.00, and 0.98 for Africa, South America, and western Pacific, respectively (Table 2). The persistent lower reflectivity strongly suggests that the contamination may not be the reason for the relatively low reflectivity over the western Pacific. In other words, highly reflective clouds found over the western Pacific are generally darker compared to the two continental regions.

PDF distributions of R_e of the DCCs for the three regions are given in Fig. 2d. The overall shapes, showing a type of normal distribution, are similar to each other; but the

AMTD
8, 2409–2436, 2015

R_e modes are evidently different between the western Pacific and tropical land regions. SDs are about 1.2 µm for all three distributions, but average values are 24.8, 22.4 µm, and 22. µm for the western Pacific, Africa, and South America, respectively, delineating relatively larger particles over the western Pacific. Because backward scattering tends to decrease while forward scattering slightly increases with respect to particle size, the difference in R_e can also be considered as one of the reasons causing the regionally different DCC reflectivity over the tropical latitudes. Note that MODIS-derived cloud parameters such as COT and R_e are based purely on visible and near-infrared radiance measurements (King et al., 1997). Thus, if measured radiances are smaller, especially for the 0.645 µm and 2.12 µm bands in the first place, smaller COT and/or larger R_e of DCCs can arise from those measurements, as was also suggested by Doelling et al. (2013a). However, since MODIS-derived cloud properties cannot be independent of measured radiances themselves on focus, it should be difficult to examine measured characteristics from their derived properties. Because of this reasoning, we further use CloudSat and CALIPSO measurements to find possible causes.

3.2 CloudSat observations and derived cloud products

To avoid circular interpretation in the use of MODIS cloud products, we first use CloudSat measurements to examine the regionally varying characteristics of tropical DCCs causing the different reflectivities.

3.2.1 Radar reflectivity profiles

The radar reflectivity profile is a fundamental observation of CloudSat that allows the examination of the vertical structure of DCC clouds. Two-dimensional histograms of the radar reflectivity for DCCs over Africa, South America, and the western Pacific and their corresponding mean profiles are given in Fig. 3. The two-dimensional distributions show similar parabolic shapes, but substantial differences exist between the western Pacific and the two continental regions, especially in the altitudes from 7 to 15 km

AMTD
8, 2409–2436, 2015

(Fig. 3a–c). These features are more evident in the averaged profiles (Fig. 3d). Large radar echoes (e.g., greater than 10 dBZ) more frequently observed in the 7–15 km layer of DCCs over the continental regions, in comparison to the western Pacific counterpart. Moreover, maximum values of radar reflectivity for DCCs over the continental regions are located at relatively high altitudes (i.e., 9–10 km compared to 7–8 km). The larger reflectivity in the higher altitudes over the tropical continental areas implies stronger convective updraft there, as in large radar echoes introduced as a proxy of strong convection (Liu et al., 2007; Luo et al., 2008; Luo et al., 2011). These results are consistent with the finding that typical updrafts over the African Congo region are stronger than those over the tropical Pacific, and so lift larger particles into high altitudes (Liu and Zipser 2005; Zipser et al., 2006; Liu et al., 2007).

CloudSat reflectivities of 0 or 10 dBZ are often used for tracing the precipitation-size particles within convective clouds (Stephens and Wood 2007). Here, to further examine DCC structure and related convection intensity, cloud top height is determined for each sample using the radar reflectivity threshold of −28 dBZ (Stephens et al., 2008). The highest altitudes showing radar reflectivities of −10, 0, and 10 dBZ (hereafter referred to as −10 dBZ height, 0 dBZ height, and 10 dBZ height) are also obtained. Average distributions are calculated from the obtained heights, −10, 0, and 10 dBZ heights, for the three analysis regions, and the results are given in Fig. 4. The mean distributions of cloud top heights for the DCCs show that the DCCs are in general slightly higher over the western Pacific compared to the African and South American regions (Fig. 4a). This result is consistent with the more frequent occurrence of cold clouds over the western Pacific (Fig. 2a). When the distributions of the highest altitudes showing −10, 0, and 10 dBZ reflectivities are compared, the difference appears to be more pronounced as the observed radar signal becomes larger. The distributions of −10 dBZ height seem to be similar among three regions (Fig. 4b). 0 dBZ heights for the western Pacific appear to be generally lower than those of the other two regions, and a substantial portion exists even at levels below 12 km. The two land regions show a nearly identical distribution. In the case of the 10 dBZ height, a much broader distribution, with a peak

AMTD
8, 2409–2436, 2015

located at the relatively low altitude of about 10 km, is apparent in the western Pacific DCCs compared to the land regions. Thus, radar reflectivity showing a relatively larger value (here 10 dBZ) appears at a comparatively lower level over the western Pacific region compared to Africa and South America. Overall, the upper part of DCCs over the western Pacific may be less dense because the 0 and 10 dBz heights are lower in spite of generally taller cloud compared to DCCs over tropical land regions. In other words, because the CloudSat radar reflectivity is proportional to the summed sixth-power of geometric particle size, the larger radar reflectivity in the upper part of clouds over the two land regions can be interpreted as either a larger amount of ice particles or larger sizes of ice there.

3.2.2 Profiles of ice water content (IWC)

As cloud particles have a direct effect on scattering and thus reflectivity, we examine the vertical distribution of IWC of DCCs collected over the three selected regions. Two-dimensional histograms of IWC and its mean vertical profiles are given in Fig. 5. Significant land–ocean contrast is evident in the IWC profiles; a much broader IWC range is shown over the two continental regions compared with the narrower IWC distribution over the western Pacific region. A majority of IWC over the western Pacific appears to have values smaller than 200 mg m^{-3} whereas there are much wider IWC distributions over two land regions up to 800–1000 mg m^{-3}, especially in layers below about 13 km.

The mean profiles of IWC of DCCs over the three regions summarize the tropical land–ocean contrast discussed above. IWC profiles appear to be similar in the upper part of the DCC layer (i.e., above 15 km). The differences in IWC between land and ocean and between the two land regions become substantial in layers below 15 km. The largest mean IWCs are shown over the South American region, and their magnitudes are as much as twice those for the western Pacific. The African region also shows a larger amount of IWC compared to that over the western Pacific, although values are smaller than those over the South American region. Overall, the zonal mean

AMTD
8, 2409–2436, 2015

profile manifests that the total amount of ice water for DCCs over the western Pacific is much smaller than those in the two continental regions and that the level showing the maximum value is lower over the western Pacific.

3.2.3 Profiles of effective radius (R_e) for ice particles

Figure 6 represents CloudSat-derived R_e profiles for DCCs over the three regions. It is noted that the narrower R_e range with smaller particles in the upper part of DCC tends to become wider with larger particles in the lower layers. It is also of interest to note that maximum occurrence levels are significantly different between the land and ocean regions; maximum occurrences for the western Pacific are at about 15 km with particle sizes of 30–50 µm, but the two land regions show maximum occurrences at lower and thicker layers below 13 km with particle sizes larger than 100 µm.

The generally increasing tendency of R_e with decreasing altitude is more evident in the averaged profiles (Fig. 6d). Even though a slight difference exists between the two land regions (i.e., African and South American domains) in the layer between 15 and 11 km, the two R_e profiles are similar to each other, but these are clearly different from that of the western Pacific. In summary, R_e for ice particles over the western Pacific is substantially smaller than those found for the two land regions, especially below the altitude of 15 km. These CloudSat results in effective radius appear to contradict the MODIS results in Fig. 2d, which show a much smaller radius range (e.g., hardly larger than 30 µm) and rather larger sizes over the western Pacific. Furthermore, the gradual increase in particle sizes from South America to Africa and the western Pacific appears to be opposite to the result found from the CloudSat retrievals.

3.2.4 Profiles of extinction coefficient (k_{ext})

k_{ext} in the visible band enables us to interpret features of cloud reflectivity at the TOA because COT is proportional to reflectivity and can be obtained by vertically integrating k_{ext} in the cloud layer. As in Eq. (1), k_{ext} in each layer can be determined from IWC

AMTD
8, 2409–2436, 2015

and R_e, thus larger k_{ext} implies larger IWC, smaller effective radius, or both. Thus, the DCC optical properties of a smaller amount of ice water and smaller particle sizes over the western Pacific region determined from CloudSat measurements seem to have a compensating effect on k_{ext}. The resultant k_{ext} profiles associated with ice water of DCCs are given in Fig. 7. The figure shows that the general patterns of the k_{ext} profiles are very similar to the IWC profiles in Fig. 5, suggesting that the effect from different radius between land and ocean regions and between Africa and South America is minor. In other words, k_{ext} is controlled largely by the amount of ice water content.

In the average profiles (Fig. 7d), k_{ext} over the western Pacific is much smaller than those over Africa and South America, again similar to the IWC profiles. These results strongly suggest that among the three analysis domains reflectivity is lowest over the western Pacific, mainly because of the smaller amount of ice cloud particles there, compared to the tropical continental African and South American regions.

3.3 CALIPSO-derived ice water path (IWP) and COT

As CALIPSO uses a visible wavelength, it can observe optical properties related to small particles such as ice crystals, but observation is limited to small optical thickness because of the fast attenuation of emitted radiation. DCC heights determined from CALIPSO are relatively high, up to 2 km, compared to CloudSat-determined DCC heights, and CALIPSO observation is generally available for only a 1–3 km depth below the CALIPSO-determined cloud top in the case of convective clouds (not shown). The cloud depth detectable from CALIPSO measurements tends to be slightly thicker over the western Pacific than over the central Africa and South America regions (not shown), suggesting that ice water density of the upper part of DCCs over the western Pacific is lower than that in the other two regions.

In order to investigate features of optical properties above the CloudSat-detected cloud top, IWP and COT are calculated by vertically integrating CALIPSO-derived layer-mean IWC and k_{ext} profiles, respectively. PDF distributions for IWP and COT are given in Fig. 8. The figure shows that all the PDF distributions are nearly similar despite the

AMTD
8, 2409–2436, 2015

more fluctuating pattern found for Africa that is probably an effect of the smaller sample size. The similarity of the PDFs found among the three analysis domains strongly suggests that the contribution from ice particles above the CloudSat-determined cloud top to the regionally different reflectivity is minor. Furthermore, magnitudes of IWP and COT seem too small when a majority of DCCs shows COT larger than 100 (Fig. 2). Thus, the contribution of ice particles residing in the uppermost layers of DCCs, only detected by CALIPSO measurements, to the regional difference of reflectivity should be insignificant.

4 Conclusions and discussion

It has been reported that DCCs over the tropical western Pacific are generally darker (i.e., lower reflectivity) compared with the reflectivities of DCCs over tropical Africa and South America. In order to examine the main cause of the lower reflectivity over the western Pacific, we first examined the regional differences in cloud optical properties observed in satellite measurements of MODIS (Aqua), CloudSat, and CALIPSO.

In doing so, DCC was defined as cloud whose cloud top temperature is colder than 205 K (i.e., $TB_{11} < 205$ K). From the MODIS-derived DCCs collected from the four January months of the 2007–2010 period, it was shown that the DCCs found over the western Pacific are colder and darker than the DCCs found over the Africa and South America domains (198.8 K vs. 199.6 and 200.2 K, and 0.93 vs. 0.98 and 0.98). MODIS-derived COTs of DCCs showed that DCCs over the western Pacific determined by applying $TB_{11} = 205$ K as a threshold are optically thinner than those over the two land regions. This may suggest that only the criterion of $TB_{11} = 205$ K allowed more optically thinner convective/anvil-type clouds over the western Pacific region. However, considering the fact that the mean reflectivity of highly reflective clouds (i.e., $Ref_{0.6} > 0.95$) was also higher in the land regions (i.e., 0.99, 1.00, and 0.98 for Africa, South America, and the western Pacific, respectively), DCCs over the western Pacific should generally be darker compared to those over the two tropical land regions.

AMTD
8, 2409–2436, 2015

The collocated CloudSat observations revealed that heights showing large radar echoes (e.g., 10 dBZ) appear to be lower over the western Pacific. At the same time, both IWC and R_e of ice particles in DCCs are smaller over the western Pacific. Furthermore, vertical distributions of k_{ext} calculated from IWC and R_e profiles are evidently smaller over the western Pacific, possibly leading to the lower COT and then lower TOA reflectivity there. However, considering that smaller particles contribute more to the backscattered radiation, the smaller particles over the western Pacific from CloudSat measurements cannot explain the comparatively lower reflectivity. These results strongly suggest that darker DCCs over the western Pacific are mainly caused by the smaller amount of ice water content compared to those of the tropical Africa and South America regions.

The regional differences in DCC's optical properties noted in this study cast a cautionary warning for the ubiquitous use of DCCs for the solar channel calibration without taking those different factors into account. On the other hand, the results also suggest a way how DCC samples can be better selected over the western Pacific for the solar channel calibration. For instance, instead of using the same criteria to determine the DCCs everywhere over the globe (e.g. TB_{11} = 205 K), regionally different criteria at least between the land and ocean can be introduced. It is because, as shown in Fig. 2 and Table 2, the use of more stringent criteria of TB_{11} = 195 K over the western Pacific area may bring in DCCs, which are comparable, in terms of their occurrence and reflectivity, to those from the use of TB = 205 K over South America or Africa.

Acknowledgements. This work was funded by the Korea Meteorologial Administration Research and Development Program under grant CATER 2012-2061.

References

Aumann, H. H., Pagano, T., and Hofstadter, M.: Observations of deep convective clouds as stable reflected light standard for climate research: AIRS evaluation, Atmospheric and Envi-

AMTD
8, 2409–2436, 2015

ronmental Remote Sensing Data Processing and Utilization III: Readiness for GEOSS, Proc. SPIE, 6684, 668410, doi:10.1117/12.734599, 2007.
Barnes, R., Eplee, R., Patt, F., Kieffer, H., Stone, T., Meister, G., Butler, J., and McClain, C.: Comparison of SeaWiFS measurements of the moon with the U.S. Geological Survey lunar model, Appl. Optics, 43, 5838–5854, doi:10.1364/AO.43.005838, 2004.
Cao, C., Vermote, E., and Xiong, X.: Using AVHRR lunar observations for NDVI long-term climate change detection, J. Geophys. Res., 114, D20105, doi:10.1029/2009JD012179, 2009.
Chun, H.-W., and Sohn, B. J.: Climatological assessment of desert targets over East Asia–Australian region for the solar channel calibration of geostationary satellites, Asia-Pac. J. Atmos. Sci., 50, 239–246, doi:10.1007/s13143-014-0012-y, 2014.
Chun, H.-W., Sohn, B. J., Kim, D.-H., Ahn, M.-H., and Ou, M.-L.: Solar channel calibration using desert targets in Australia: application to the MTSAT-1R visible sensor, J. Meteorol. Soc. Jpn., 90, 191–205, 2012.
Doelling, D. R., Hong, G., Morstad, D., Bhatt, R., Gopalan, A., and Xiong, X.: The characterization of deep convective cloud albedo as a calibration target using MODIS reflectances. Earth Observing Missions and Sensors: Development, Implementation, and Characterization, edited by: Xiong, X., Kim, C., and Shimoda, H., International Society for Optical Engineering, Proc. SPIE, 7862, 786201, doi:10.1117/12.869577, 2010.
Doelling, D. R., Morstad, D., Scarino, B. R., Bhatt, R., and Gopalan, A.: The characterization of deep convective clouds as an invariant calibration target and as a visible calibration technique, IEEE T. Geosci. Remote, 51, 1147–1159, doi:10.1109/TGRS.2012.2225066, 2013a.
Doelling. D. R., Scarino, B. R., Morstad, D., Gopalan, A., Bhatt, R., Lukashin, C., and Minnis, P.: The intercalibration of Geostationary visible Imagers using operational hyperspectral SCIAMACHY radiances, IEEE T. Geosci. Remote, 51, 1245–1254, doi:10.1109/TGRS.2012.2227760, 2013b.
Govaerts, Y. M. and Clerici, M.: Evaluation of radiative transfer simulations over bright desert calibration sites, IEEE T. Geosci. Remote, 42, 176–187, 2004.
Ham, S.-H., Sohn, B.-J., Yang, P., and Baum, B. A.: Assessment of the quality of MODIS cloud products from radiance simulations, J. Appl. Meteorol. Clim., 48, 1591–1612, 2009.
Ham, S.-H. and Sohn, B. J.: Assessment of the calibration performance of satellite visible channels using cloud targets: application to Meteosat-8/9 and MTSAT-1R, Atmos. Chem. Phys., 10, 11131–11149, doi:10.5194/acp-10-11131-2010, 2010.

AMTD
8, 2409–2436, 2015

Ham, S.-H., and Sohn, B. J.: vertical-homogeneity assumption causing inconsistency between visible- and infrared-based cloud optical properties, IEEE Geosci. Remote Sense., 9, 531–535, 2012.
Heymsfield, A. J., Winker, D., and van Zadelhoff, G.-J.: Extinction-ice water content-effective radius algorithms for CALIPSO, Geophys. Res. Lett., 32, L10807, doi:10.1029/2005GL022742, 2005.
Kahn, B. H., Chahine, M. T., Stephens, G. L., Mace, G. G., Marchand, R. T., Wang, Z., Barnet, C. D., Eldering, A., Holz, R. E., Kuehn, R. E., and Vane, D. G.: Cloud type comparisons of AIRS, CloudSat, and CALIPSO cloud height and amount, Atmos. Chem. Phys., 8, 1231–1248, doi:10.5194/acp-8-1231-2008, 2008.
Kim, B.-R., Ham, S.-H., Kim, D.-H., and Sohn, B. J.: Post-flight radiometric calibration of the Korean geostationary satellite COMS Meteorological Imager, Asia-Pac. J. Atmos. Sci., 50, 201–210, doi:10.1007/s13143-014-0008-7, 2014.
King, M. D., Tsay, S.-C., Platnick, S., Wang, M., and Liou, K.-N.: Cloud retrieval algorithms for MODIS: optical thickness, effective particle radius, and thermodynamic phase, MODIS Algorithm Theoretical Basis Document ATBD-MOD-05, 83 pp., 1997.
Lin, B. and Rossow, W. B.: Observations of cloud liquid water path over oceans: optical and microwave remote sensing methods, J. Geophys. Res., 99, 20907–20927, doi:10.1029/94JD01831, 1994.
Liu, C. and Zipser, E. J.: Global distribution of convection penetrating the tropical tropopause, J. Geophys. Res., 110, D23104, doi:10.1029/2005JD006063, 2005.
Liu, C., Zipser, E. J., and Nesbitt, S. W.: Global distribution of tropical deep convection: different perspectives form TRMM infrared and radar data, J. Climate, 20, 489–503, 2007.
Luo, Y., Zhang, R., Qian, W., Luo, Z., and Hu, X.: Intercomparison of deep convection over the Tibetan Plateau-Asian monsoon region and subtropical North America in boreal Summer using CloudSat/CALIPSO data, J. Climate, 24, 2164–2177, 2011.
Luo, Z., Liu, G. Y., and Stephens, G. L.: CloudSat adding new insight into tropical penetrating convection, Geophys. Res. Lett., 35, L19819, doi:10.1029/2008GL035330, 2008.
Mace, G. G., Marchand, R., Zhang, Q., and Stephens, G.: Global hydrometeor occurrence as observed by CloudSat: initial observations from summer 2006, Geophys. Res. Lett., 34, L09808, doi:10.1029/2006GL029017, 2007.

AMTD
8, 2409–2436, 2015

Miesch, C., Cabot, F., Briottet, X., and Henry, P.: Assimilation method to derive spectral ground reflectance of desert sites from satellite datasets, Remote Sens. Environ., 87, 359–370, 2003.

Parkinson, C. L.: Aqua: an earth-observing satellite mission to examine water and other climate variables, IEEE T. Geosci. Remote, 41, 173–183, 2003.

Sohn, B.-J., Ham, S.-H., and Yang, P.: Possibility of the visible-channel calibration using deep convective clouds overhooting the TTL, J. Appl. Meteorol. Clim., 48, 2271–2283, 2009.

Stephens, G. L., Deborah G. Vane, D. G., Boain, R. J., Mace, G. G., Sassen, K., Wang, Z., Illingworth, A. J., O'Connor, E. J., Rossow, W. B., Durden, S. L., Miller, S. D., Austin, R. T., Benedetti, A., Mitrescu, C., and The CloudSat Science Team: The CloudSat mission and the A-Train: a new dimension of space-based observations of clouds and precipitation, B. Am. Meteorol. Soc., 83, 1771–1790, doi:10.1175/BAMS-83-12-1771, 2002.

Stephens, G. L. and Wood, N. B.: Properties of tropical convection observed by millimeter-wave radar systems, Mon. Weather Rev., 135, 821–842, 2007.

Stephens, G. L. and Coauthors: CloudSat mission: performance and early science after the first year of operation, J. Geophys. Res., 113, D00A18, doi:10.1029/2008JD009982, 2008.

Stercks, S., Livens, S., and Adriaensen, S.: Rayleigh, deep convective clouds, and cross-sensor desert calibration validation for the PROBA-V mission, IEEE T. Geosci. Remote, 51, 1437–1452, doi:10.1109/TGRS.2012.2236682, 2013.

Winker, D. M., Pelon, J., and McCormick, M. P.: The CALIPSO mission: spaceborne lidar for observation of aerosols and clouds. Lidar Remote Sensing for Industry and Environment Monitoring III, edited by: Singh, U. N., Itabe, T., and Liu, Z., International Society for Optical Engineering, SPIE Proceedings, Vol. 4893, 1–11, 2003.

Wood, N.: Level 2B Radar-Visible Optical Depth Cloud Water Content (2B-CWC-RVOD) process description document, Cooperative Inst. Res. Atmosphere (CIRA), Fort Collins, CO, Rep. Version 5.1, October 2008.

Young, S. A. and Vaughan, M. A.: The retrieval of profiles of particulate extinction from cloud-aerosol lidar infrared pathfinder satellite observations (CALIPSO) data: algorithm description, J. Atmos. Ocean. Tech., 26, 1105–1119, 2009.

Zipser, E. J., Cecil, D., Liu, C., Nesbitt, S., and Yorty, D.: Where are the most intense thunderstorms on earth?, B. Am. Meteorol. Soc., 87, 1057–1071, 2006.

AMTD
8, 2409–2436, 2015

Table 1. The numbers of MODIS-CloudSat collocated DCC pixels over the three analysis regions.

	Africa	South America	Western Pacific
2007JAN	217	248	768
2008JAN	8	199	577
2009JAN	22	187	634
2010JAN[a]	38	53	398
Total	285	687	2377

[a] 2010JAN: only 15 days are available (due to the battery problem of CloudSat).

AMTD
8, 2409–2436, 2015

Table 2. Mean $Ref_{0.6}$ and TB_{11} of selected DCC pixels for the three regions. Values in the parentheses are from samples satisfying $Ref_{0.6} > 0.95$. $Ref_{0.6}$ represents the MODIS reflectivity at the 0.645 µm band, and TB_{11} represents the MODIS brightness temperature at the 11 µm band.

	Africa		South America		Western Pacific	
	$Ref_{0.6}$	TB_{11}	$Ref_{0.6}$	TB_{11}	$Ref_{0.6}$	TB_{11}
2007JAN	0.98	199.2	1.00	200.7	0.92	198.7
	(0.99)	(198.8)	(1.00)	(200.6)	(0.98)	(197.0)
2008JAN	1.00	202.8	1.00	199.4	0.93	199.7
	(1.00)	(202.8)	(1.01)	(199.2)	(0.98)	(198.5)
2009JAN	0.95	198.6	0.94	199.8	0.96	197.9
	(0.99)	(197.1)	(0.99)	(199.6)	(0.99)	(196.5)
2010JAN	0.98	201.3	0.90	202.3	0.90	199.3
	(0.99)	(201.6)	(1.00)	(201.0)	(0.97)	(197.6)
Total	0.98	199.6	0.98	200.2	0.93	198.8
	(0.99)	(199.1)	(1.00)	(200.0)	(0.98)	(197.2)

AMTD
8, 2409–2436, 2015

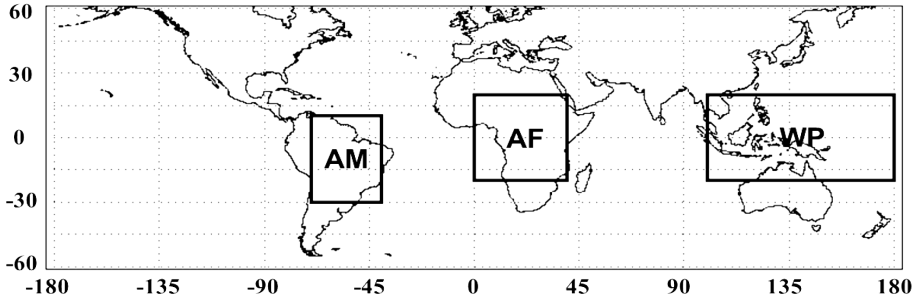

Figure 1. Analysis domains used in this study. AM, AF, and WP represent South America, Central Africa, and the western Pacific domains, respectively.

AMTD
8, 2409–2436, 2015

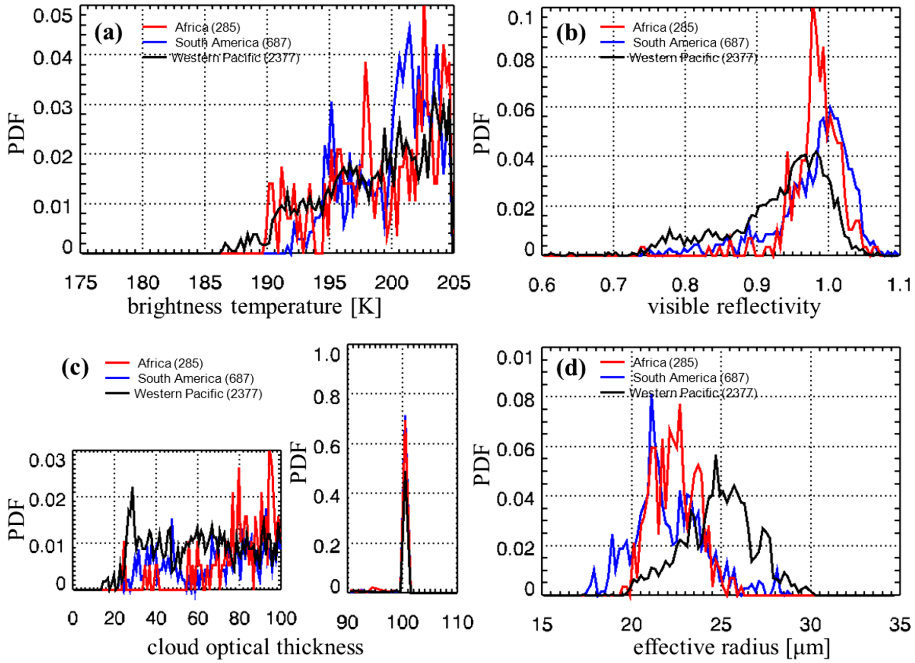

Figure 2. Distributions of PDFs of **(a)** brightness temperature at 11 μm, **(b)** reflectance at 0.645 μm observed by MODIS, and **(c)** cloud optical thickness, and **(d)** effective radius from MODIS products. The red, blue, and black solid lines represent DCCs observed over Africa, South America, and the western Pacific analysis domains, respectively.

AMTD
8, 2409–2436, 2015

A cautionary use of DCC as a solar calibration target

M.-J. Choi and B. J. Sohn

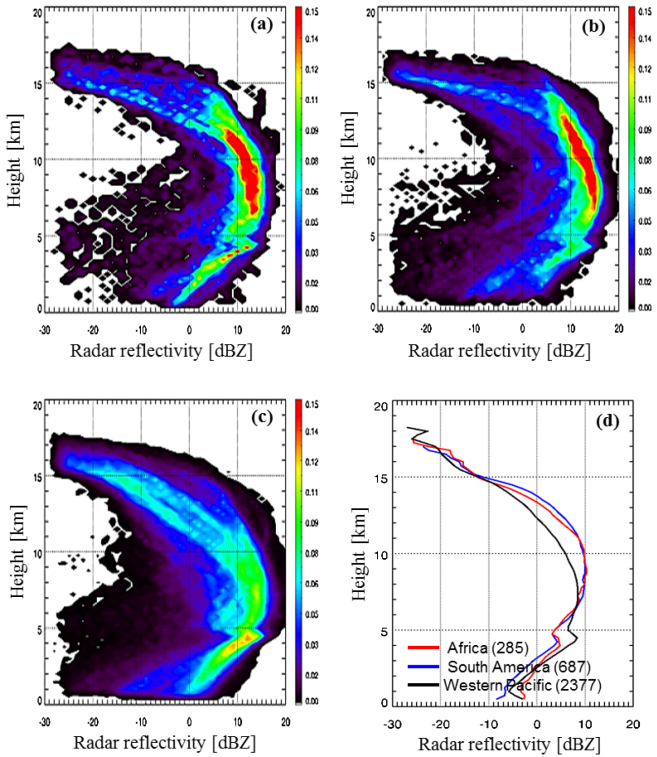

Figure 3. Two-dimensional histograms of radar reflectivity profiles for DCCs observed over the **(a)** Africa, **(b)** South America, and **(c)** western Pacific domains. The color bars in **(a)**, **(b)**, and **(c)** represent probability with respect to the total profiles. Average profiles of the radar reflectivity for the three domains are given in **(d)**, and the number given in the parentheses represents the number of profiles used for the average.

AMTD
8, 2409–2436, 2015

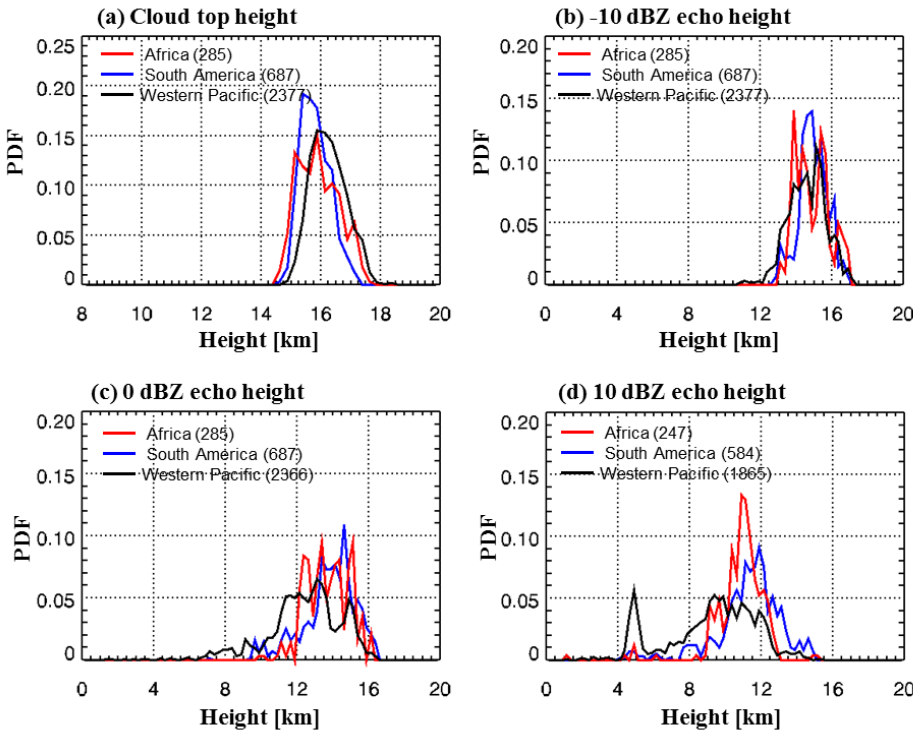

Figure 4. PDF distributions of **(a)** cloud top height and of echo heights showing **(b)** −10, **(c)** 0, and **(d)** 10 dBZ in DCC samples. The numbers given in the parentheses represent the number of profiles falling in each category.

AMTD
8, 2409–2436, 2015

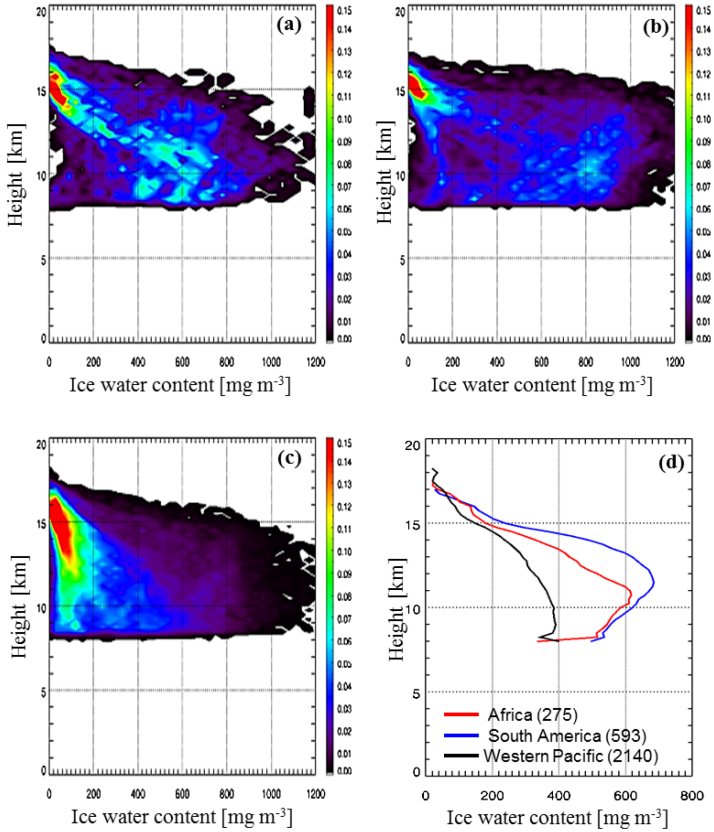

Figure 5. Same as Fig. 3 but for CloudSat-derived ice water content.

AMTD
8, 2409–2436, 2015

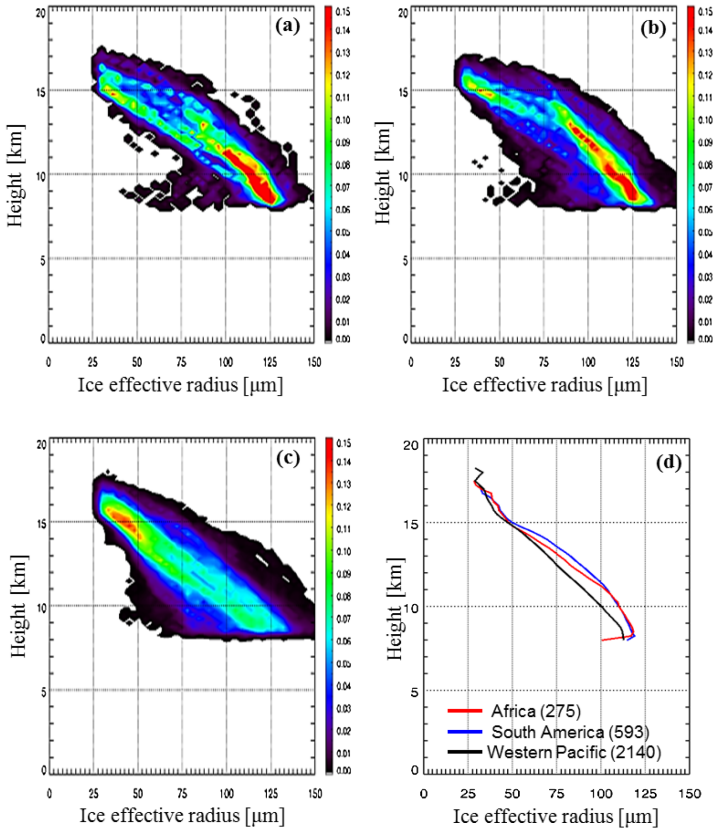

Figure 6. Same as Fig. 3 but for ice effective radius.

AMTD
8, 2409–2436, 2015

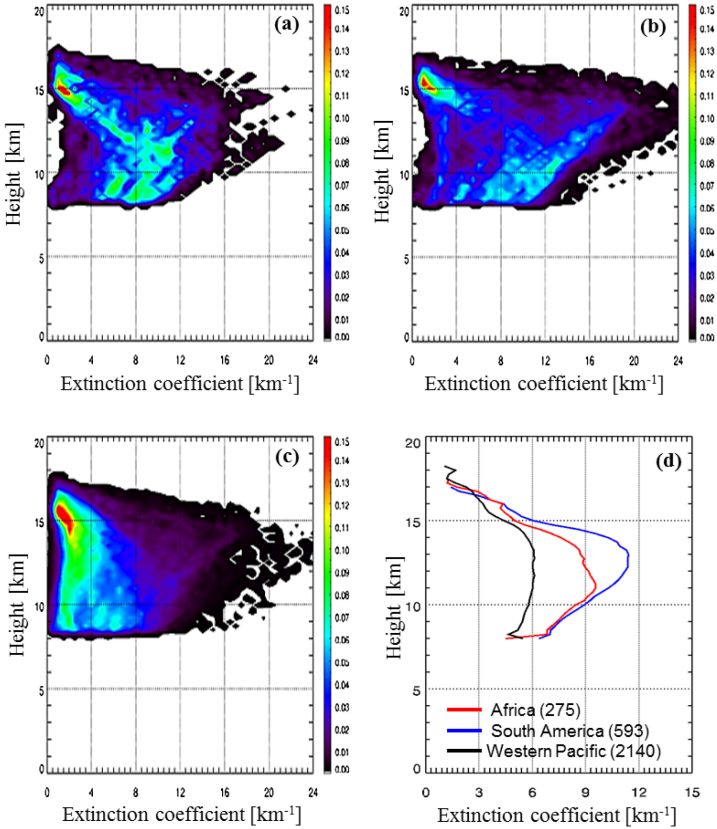

Figure 7. Same as Fig. 3 but for extinction coefficient.

AMTD
8, 2409–2436, 2015

A cautionary use of DCC as a solar calibration target

M.-J. Choi and B. J. Sohn

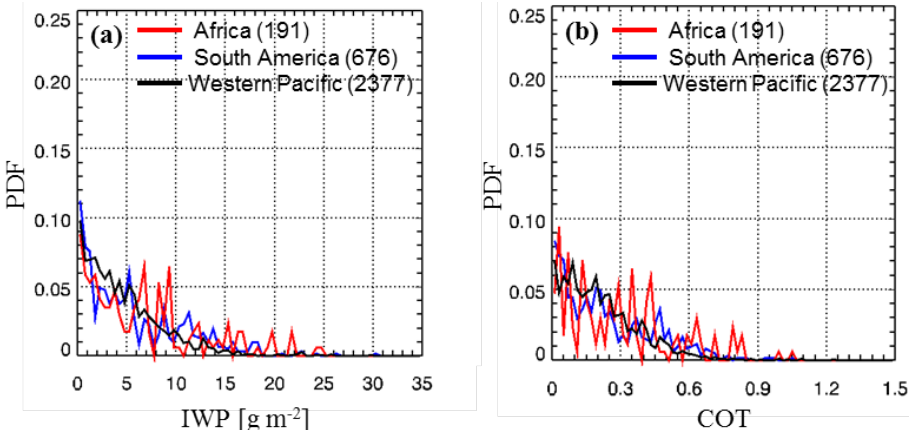

Figure 8. PDF distributions of CALIPSO-estimated **(a)** ice water path (IWP) and **(b)** cloud optical thickness (COT).

AMTD
8, 2409–2436, 2015